analytical chemistry

Article

pubs.acs.org/ac

Low-Power Miniaturized Helium Dielectric Barrier Discharge Photoionization Detectors for Highly Sensitive Vapor Detection

Hongbo Zhu,[†,‡] Menglian Zhou,[†,‡] Jiwon Lee,[†,‡] Robert Nidetz,[‡,§] Katsuo Kurabayashi,[‡,§] and Xudong Fan*[,†,‡]

[†]Department of Biomedical Engineering, University of Michigan, 1101 Beal Avenue, Ann Arbor, Michigan 48109, United States

[‡]Center for Wireless Integrated MicroSensing and Systems (WIMS^2), University of Michigan, Ann Arbor, Michigan 48109, United States

[§]Department of Mechanical Engineering, University of Michigan, 2350 Hayward, Ann Arbor, Michigan 48109, United States

Supporting Information

ABSTRACT: This paper presents the design, fabrication, and characterization of a microhelium dielectric barrier discharge photoionization detector (μHDBD-PID) on chip with dimensions of only ~15 mm × ~10 mm × ~0.7 mm and weight of only ~0.25 g. It offers low power consumption (<400 mW), low helium consumption (5.8 mL/min), rapid response (up to ~60 ms at a flow rate of 1.5 mL/min), quick warm-up time (~5 min), an excellent detection limit (a few picograms), a large linear dynamic range (>4 orders of magnitude), and maintenance-free operation. Furthermore, the μHDBD-PID can be driven with a miniaturized (~5 cm × ~2.5 cm × ~2.5 cm), light (22 g), and low cost (~$2) power supply with only 1.5 VDC input. The dependence of the μHDBD-PID performance on bias voltage, auxiliary helium flow rate, carrier gas flow rate, and temperature was also systematically investigated. Finally, the μHDBD-PID was employed to detect permanent gases and a sublist of the EPA 8260 standard reagents that include 51 analytes. The μHDBD-PID developed here can have a broad range of applications in portable and microgas chromatography systems for *in situ*, real-time, and sensitive gas analysis.

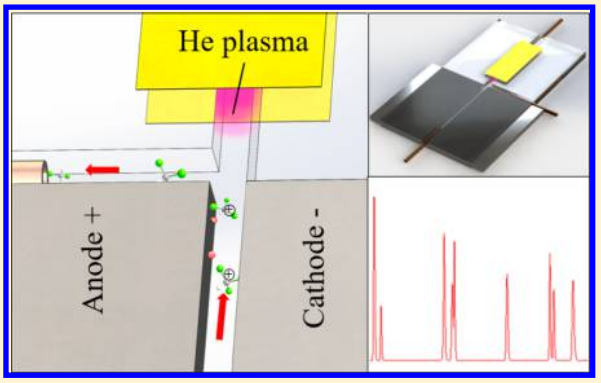

Photoionization detectors (PIDs) are being widely used in gas chromatography (GC) systems due to their high sensitivity and large dynamic range.[1−3] In a typical design, a PID consists of a vacuum UV (VUV) lamp filled with low-pressure rare gases such as xenon, krypton, and argon, which generate photons ranging from 9.6 to 11.8 eV, and a sealing window made of a UV transparent crystal (*e.g.*, LiF, MgF_2, and CaF_2). However, those PIDs suffer from a very limited lifetime of a few hundred to a couple of thousand hours and gradual performance degradation due to gas leakage and window degradation caused by crystal solarization, water etching, and contamination of chemical compounds.[4] Thus, constant maintenance and calibration are needed during their entire operation lifetime. Furthermore, although those PIDs are able to provide sufficient photon energy (*e.g.*, 11.8 eV by argon based PIDs with a LiF window) to ionize most of chemical compounds, there still exist many important compounds with the ionization potential (IP) above or close to 11.8 eV, such as Freon (IP: 11.77 eV to 12.91 eV), methane (IP: 12.98 eV), chlorine trifluoride (IP: 12.65 eV), dichlorofluoromethane (IP: 12.39 eV), phosgene (IP: 11.77 eV), and ethane (IP: 11.65 eV), just to name a few, which cannot be analyzed with those PIDs.

Atmospheric pressure rare gas discharge based PIDs usually have a windowless design, which maximizes UV transmission and can potentially extend the PID lifetime. Helium is typically used in this type of PID. Known as Hopfield emission, which results from the transition from the diatomic helium state to the dissociative helium state, photons ranging from 13.5 to 17.5 eV can be generated during the helium discharge process, making the helium discharge PID (HD-PID) virtually a universal detector for gas analysis.[5] In an HD-PID, helium plasma is usually generated by direct current (DC) discharge,[6−8] pulsed discharge,[5,9−19] or dielectric barrier discharge (DBD).[20−23] DC discharge relies on high voltage (or electric field) to break down helium into positive ions and electrons, thus generating gas plasma.[24] Recently, a miniaturized HD-PID based on DC discharge was demonstrated with 550 VDC across a 20 μm gap and power consumption of only 1.4 mW.[7,8,25] A detection limit on the order of 10 pg was achieved.[8] Pulsed discharge is also called pulsed DC discharge. The operation principle is similar to DC discharge but uses 1 kHz to 1 MHz pulses to lower average power consumption and achieve better and more stable ionization/excitation.[24] The popular PIDs from Valco Instru-

Received: June 3, 2016
Accepted: August 17, 2016
Published: August 25, 2016

DOI: 10.1021/acs.analchem.6b02180
Anal. Chem. 2016, 88, 8780−8786

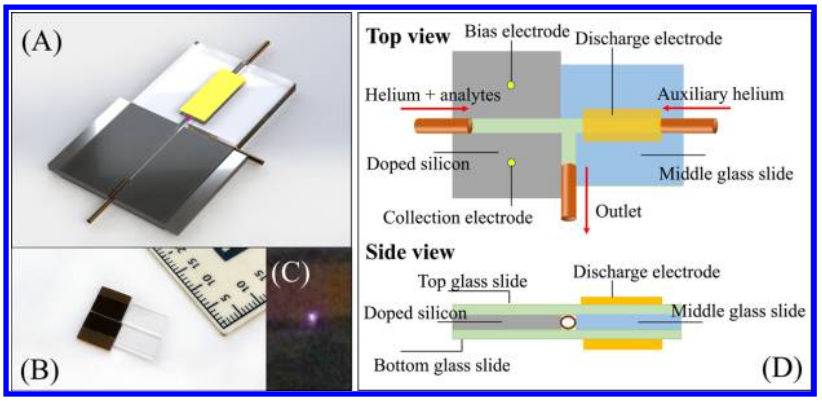

Figure 1. (A) 3-dimensional rendering of a microhelium discharge photoionization detector (μHDBD-PID). (B) Picture of a μHDBD-PID (without the discharge electrodes) and plasma generated by a μHDBD-PID. (C) Plasma generated by a μHDBD-PID (most of the plasma was blocked by the electrode). Detailed structure of a μHDBD-PID. See also Figure S1 for all dimensions.

ments are based on the pulsed discharge technology.[5,10−12,18,19] Recently, a micropulsed discharge PID was also developed with the size as large as 10 cm^3 and a detection limit of a few picograms.[13,26] However, one of the major drawbacks of DC discharge is the sputtering effect; that is, high-speed ions continuously bombard the cathode material,[24] which limits the lifetime of the detector and requires constant maintenance of electrodes and chambers (such as electrode replacement and discharge chamber cleaning). For pulsed discharge, since the duty cycle and, hence, the average electrical power are lower, the overall sputtering effect is lower. However, due to high instantaneous power, the sputtering cannot be completely prevented.

DBD uses high-voltage (1−100 kV), high-frequency (up to a few MHz) potential to generate atmospheric pressure plasma. In a DBD design, dielectric materials (*e.g.*, glass, polymer, quartz, *etc.*) are placed on the electrode surface facing the discharge chamber, thus forming a protection layer.[24] Compared to the two aforementioned discharge methods, the DBD method is advantageous in a homogeneous discharge[24,27] and at very long electrode operation lifetime. Therefore, it has become the preferred method for atmospheric pressure plasma generation and been applied in numerous applications.[28−33] Recently, a few DBD based helium discharge PIDs became commercially available (such as BID-2010 Plus from Shimadzu and DBDID from ABB Inc.) with the detection limit ranging from a few tens of picogram to subpicogram.[34] However, the existing DBD based HD-PIDs (such as BID-2010 Plus and DBDID) are bulky (similar to the dimensions and weight of a commercial FID) and power intensive (DBDID: 12 W) and require a large auxiliary helium flow rate (50−100 mL/min) and long warm-up time. While those HD-PIDs can be used in benchtop GC systems, they are not suitable for portable or micro-GC systems for field applications.

In this paper, we developed a microhelium dielectric barrier photoionization detector (μHDBD-PID) on chip with dimensions of only ∼15 mm × ∼10 mm × ∼0.7 mm and weight of only ∼0.25 g. It offers low power consumption (<400 mW), low helium consumption (5.8 mL/min), rapid response (as good as FID), quick warm-up time (∼5 min), an excellent detection limit (a few pg), a large linear dynamic range (>4 orders of magnitude), and maintenance-free operation. Furthermore, the μHDBD-PID can be driven with a miniaturized (∼5 cm × ∼2.5 cm × ∼2.5 cm), light (22 g), and low cost (∼$2) power supply with only 1.5 VDC input. Here we report the design, fabrication, and characterization of the above μHDBD-PID and demonstrate its GC applications. A detailed comparison of our μHDBD-PID with other HD-PIDs is summarized in Table S1.

DEVICE FABRICATION AND ASSEMBLY

All the silicon and glass wafers were purchased from University Wafer Company (Boston, MA). As shown in Figures 1 and S1, a 100 μm thick Borofloat 33 glass wafer (P/N 1737) was diced into 15 mm × 10 mm rectangular pieces and used as the top and bottom substrates. A 500 μm thick P-type ⟨100⟩ silicon wafer with double-side-polished 500 nm thick thermal oxide layers (P/N 2078) was diced into a 7.5 mm × 6 mm rectangular shape, followed by wet etching using 49% buffered HF to remove the oxide layer. As illustrated in Figure 1(D), two pieces of such prepared silicon wafers were then bonded onto the bottom glass substrate using UV-curable optical glue (Norland 81). The gap between the two silicon wafers was 380 μm to create a fluidic channel for analytes and carrier gas (*i.e.*, helium). Meanwhile, the two silicon wafers also acted as the bias and the collection electrodes. Borofloat 33 glass wafer (P/N 517) (500 μm thick) was diced into two rectangular pieces (7.5 mm × 4.8 mm and 7.1 mm × 4.8 mm) and then bonded using the same UV-curable glue onto the bottom glass substrate with a 380 μm gap between each other to create a fluidic channel for auxiliary helium. Another gap of 380 μm was also created between the silicon wafer and the glass wafer to form the third fluidic channel as the outlet. Finally, the top glass substrate was bonded onto the middle silicon and glass pieces using the same UV-curable optical glue. After assembly, three guard columns with 380 μm OD and 250 μm ID were inserted into the two inlets and the outlet of fluidic channels and sealed with the optical glue.

To excite helium plasma, a low-cost miniaturized high-voltage high-frequency power supply was developed in-house based on a flyback transformer circuit (shown in Figure S2(A)). It has the dimension of ∼5 cm × ∼2.5 cm × ∼2.5 cm (Figure S2(B)) and weighs about 22 g. With a 1.5 VDC input (257 mA), it outputs 4 kV at 7.7 kHz. The high-voltage output and the ground of the power supply were connected to the top and the bottom glass substrates, respectively, via two pieces of copper tapes (dimension: 5 mm × 2 mm; see Figures 1(D) and S1 for illustration).

To generate a signal, a variable DC bias voltage (nominal voltage: 40 VDC) was applied between the collection and the

DOI: 10.1021/acs.analchem.6b02180
Anal. Chem. 2016, 88, 8780−8786

bias electrodes (Figure S3). The current signal was converted to the voltage signal and amplified by an amplifier (Stanford Research Systems SR560, input impedance = 100 MΩ + 25 pF) with a gain factor of 5 and low pass cutoff frequency of 1 Hz. The final voltage signal was recorded through a LabVIEW program via a DAQ card (NI USB-6210, National Instruments, Austin, TX) with the digital low pass cutoff frequency of 25 Hz and the data acquisition rate of 14.5 Hz. The μHDBD-PID was operated at 20 °C unless otherwise specified.

EXPERIMENTAL SECTION

Methanol (P/N 322415), pentane (P/N 236705), carbon tetrachloride (P/N 289116), heptane (P/N 246654), benzene (P/N 270709), toluene (P/N 244511), ethylbenzene (P/N 03079), *p*-xylene (P/N 317195), *n*-nonane (P/N 296821), EPA 8260 VOC mix (P/N 500607), aliphatics mix (C5−C12) (P/N UST157), and Mol Sieve 5A PLOT (P/N 2423) column for permanent gas separation were all purchased from Sigma-Aldrich (St. Louis, MO) and used without further purification or treatment. Ultrapure helium (99.999%) used as auxiliary gas and carrier gas in all experiments was purchased from Cryogenic Gases (Ann Arbor, MI). GC guard column (Catalog# 10059), separation column Rtx-VMS (Catalog# 19915), and Rtx-1 (Catalog# 10105) were purchased from Restek Corp. (Bellefonte, Pa).

The experimental setup is illustrated in Figure 2. All the analytes were injected from the 1177 injector equipped on a

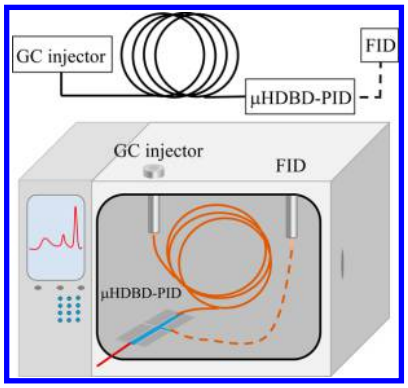

Figure 2. Experimental setup.

Varian 3800 GC with a split ratio of 100. A 1 m long guard column was used to connect the separation column and the μHDBD-PID, unless otherwise specified. The outlet of the μHDBD-PID was connected to the atmosphere. Only during the nondestruction verification was the outlet of the μHDBD-PID connected to a commercial FID equipped on a Varian 3800 GC via a short guard column. The auxiliary and carrier gas flow rates were measured at the inlets of auxiliary channel and the analyte channel, respectively, with an Ellutia-6000 GC flowmeter.

RESULTS AND DISCUSSION

Low-Voltage and Low-Power Operation. The breakdown voltage is propositional to the dietetic layer thickness[35] and the gap between the excitation electrodes.[27] In our design, the dielectric barrier is only 100 μm thick and the electrodes are only 380 μm apart, which enable the onset of helium plasma at a relatively low voltage (*i.e.*, 4 kV) and the entire operation power as low as 385 ± 3 mW (Agilent E3649A, 1.5 VDC at 257 mA). Note that the above power consumption was measured at the "no-load test" (*i.e.*, open circuit test). The actual power consumption on the μHDBD-PID by examining the difference between the open and closed circuits is approximately 3 mW, which is on the same order of magnitude as the power dissipation calculated in the next section ("Warm-up Time"). It is noted that the μHDBD-PID was designed to operate at room temperature and the power specified above was mainly for the helium discharge circuit. Extra power is needed if operation at elevated temperature is desired.

Warm-up Time. The low AC voltage and low power consumption also translate to a shorter warm-up time. The helium discharge efficiency depends on a number of factors, such as electrode gap, dielectric barrier thickness, temperature, AC frequency, voltage, *etc.*. With all other factors fixed, the temperature becomes a dominant factor in determining the plasma fluctuation. The longer it takes for the device's temperature to stabilize, the longer the warm-up time.

The excitation electrode geometry in our setup can be modeled as a capacitor. Power dissipation occurs when AC voltage is applied, which can be calculated as[36]

$$P = V^2 \omega C(DF)$$

where P is the dissipated power. V and ω are the applied AC voltage and angular frequency, respectively. C is the capacitance, and DF is the dissipation factor. At equilibrium, the dissipated power manifests itself as the increase in the device temperature.[37] Using V = 4000 V, $\omega = 2 \times \pi \times 7700$, C = 0.9 pf, and DF = 0.003, the dissipated power is calculated to be as low as 2 mW, resulting in a very small increase in device temperature and, hence, quick temperature stabilization. In fact, the temperature of the μHDBD-PID during operation was measured to be 20.7 °C with a Southwire 31030s noncontact IR thermometer, only 0.4 °C above the ambient temperature. Consequently, as shown in Figure 3, the μHDBD-PID can be stabilized within only 5 min.

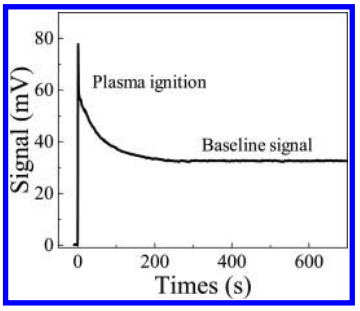

Figure 3. Plasma ignition. It took about 5 min for the μHDBD-PID to warm up and settle down. The baseline level was 32.7 mV, and the standard deviation (σ) was 0.153 mV. Bias voltage, 40 V; carrier gas flow rate, 1 mL/min; auxiliary flow pressure, 1 psi; ambient temperature, 20 °C.

Bias Voltage Optimization. Following photoionization, the ions of analytes are compelled by the electric field between the two electrodes and reach the electrodes. A strong electric field can reduce the ion flux traveling time and increase the ion collection efficiency by preventing ion recombination and quenching. However, an excessive electric field not only increases the noise without proportionately increasing the signal, but also adds costs. In order to optimize the bias voltage for the μHDBD-PID, we used 2.356 ng of heptane as a model

DOI: 10.1021/acs.analchem.6b02180
Anal. Chem. 2016, 88, 8780−8786

system. As shown in Figure 4, initially the peak height and the signal-to-noise ratio (SNR) increase when the bias voltage is in

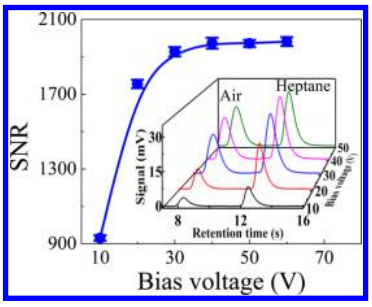

Figure 4. Signal to noise ratio (SNR) for 2.356 ng of heptane as a function of bias voltage of collection electrodes at 20 °C. The response signal is defined as the peak value of the analyte. Carrier gas flow rate was 1 mL/min. Auxiliary flow pressure was 1 psi. A 1 m Rtx-1 column was used for air and heptane separation. Error bars were obtained with four measurements. Inset: The corresponding chromatogram recorded by the μHDBD-PID. The solid curve is a cubic B-Spline interpolation and extrapolation fit to guide the eye.

the range 10−30 V, and they level off when the bias voltage is beyond 40 V. Therefore, in the following experiments, the bias voltage was set at 40 V, which is the minimum bias voltage to generate the maximal ion collection efficiency and SNR.

Flow Dependence. The intensity of plasma's deep UV emission shows a positive correlation with the auxiliary helium flow rate.[38] Consequently, the peak height (*i.e.*, signal) increases with the increased auxiliary helium flow rate, as shown in Figure 5(A). However, at an excessive auxiliary helium flow rate, plasma jet occurs, accompanied by a drastic increase in the noise level. Consequently, the SNR has a bell shape with the maximum achieved at about 16 mL/min (measured at the auxiliary flow inlet with corresponding gas source pressure: 3 psi). In the experiments that followed, we used an auxiliary helium rate of 5.8 mL/min (measured at the auxiliary flow inlet with the corresponding gas source pressure of 1 psi) in order to reduce helium consumption (but at the expense of the SNR, which is reduced by 30−40% from its maximum).

At a fixed auxiliary helium inlet pressure (1 psi in our case), changing the carrier gas flow rate also affects the performance of the μHDBD-PID, as the absolute auxiliary helium flow rate decreases when the carrier gas flow increases. Thus, with the increased carrier gas flow rate, a slight decrease in the analyte peak area can be observed (see Figure 5(B)) due to the decreased plasma emission, as discussed previously. Besides the peak area, the peak height is also affected by the carrier gas flow rate, as shown in Figure 5(B). At a low carrier gas flow rate (*e.g.*, 0.5 mL/min), the peak height for a given quantity of analyte is low due to peak broadening resulting from long elution time. On the other hand, at a very high carrier gas flow rate (*e.g.*, 3.6 mL/min), the decrease in the auxiliary helium flow rate becomes a dominant effect. Consequently, although the peak is sharper at a high carrier gas flow rate (see Figure S4), the peak height still decreases due to the decrease in plasma emission. For the current μHDBD-PID, the maximal peak height was achieved with the carrier flow rate of 1−2 mL/min (Figure 5(B)).

Overall, Figure 5 shows the interplay of the auxiliary helium flow rate and the carrier gas flow rate on the analyte peak and peak area. Since the auxiliary flow rate is usually adjusted by tuning the gas source pressure, the absolute auxiliary flow rate is affected by the carrier gas flow rate (at a given auxiliary gas source pressure). As a result, GC separation based on the pressure ramping method[8] cannot be employed if an HDBD-PID is used for quantitative analysis, unless the same auxiliary flow rate can be maintained independently of the carrier gas flow rate during the pressure ramping.

Temperature Effect. Through the previous studies,[39] it is known that temperature affects the helium discharge performance. Here we investigated the effect of temperature on the overall μHDBD-PID performance. The μHDBD-PID was heated by a thermoelectric Peltier plate (P/N CP30138 purchased from Digi-Key) from 20 to 80 °C (maximum operation temperature of the plate) for four cycles. The results shown in Figure 6 are highly repeatable in multicycle heating processes, attesting to the thermal robustness of the μHDBD-PID. As the temperature increases from 20 to 80 °C, the peak height of 2.356 ng of heptane increases 2.5 times, whereas the noise level increases slightly higher than that, resulting in a 5% decrease in the SNR. In practice, to obtain a reliable performance, the temperature of the μHDBD-PID should be kept constant and the thermal crosstalk between the separation column and the μHDBD-PID should be avoided when the temperature ramping method is used in GC separation.

Response Time. Owing to the flow-through design, μHDBD-PID has a rapid response to analytes. A comparison between the μHDBD-PID and a commercial FID was shown in Figure 7(A), showing virtually identical peak width. In fact, the

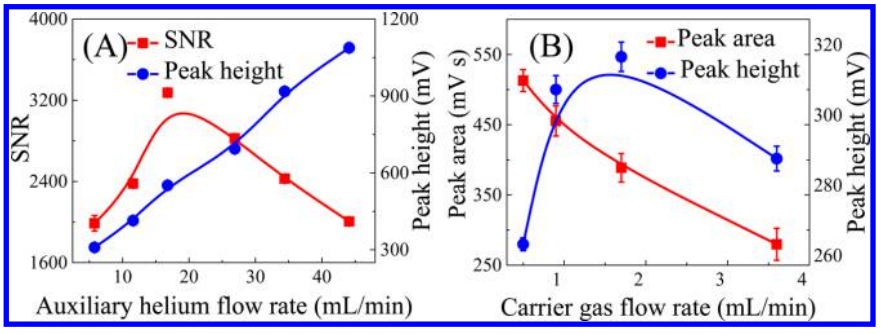

Figure 5. (A) Response signal and corresponding signal-to-noise ratio (SNR) for 2.356 ng of heptane at various auxiliary helium flow rates. Carrier gas flow was fixed at 1 mL/min. (B) Response signal and corresponding signal-to-noise ratio (SNR) for 2.356 ng of heptane at various carrier flow rates. Auxiliary helium pressure was fixed at 1 psi. A 1 m Rtx-1 column was used for air and heptane separation. The response signal is defined as the peak value of the analyte. Ambient temperature was 20 °C. Error bars were obtained with four measurements. The solid curve is a cubic B-Spline interpolation and extrapolation fit to guide the eye.

DOI: 10.1021/acs.analchem.6b02180
Anal. Chem. 2016, 88, 8780−8786

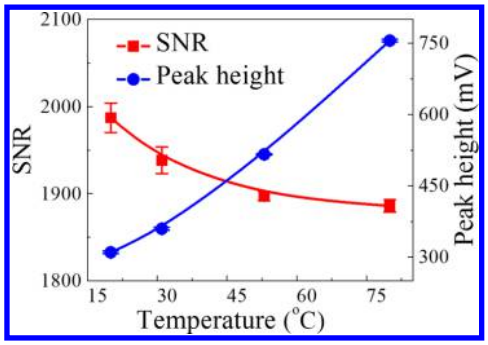

Figure 6. Response signal and corresponding signal-to-noise ratio (SNR) for 2.356 ng of heptane as a function of temperature. The response signal is defined as the peak value of the analyte. Carrier gas flow rate was 1 mL/min. Auxiliary flow pressure was 1 psi. A 1 m Rtx-1 column was used for air and heptane separation. Error bars were obtained with four measurements. The solid curve is a cubic B-Spline interpolation and extrapolation fit to guide the eye.

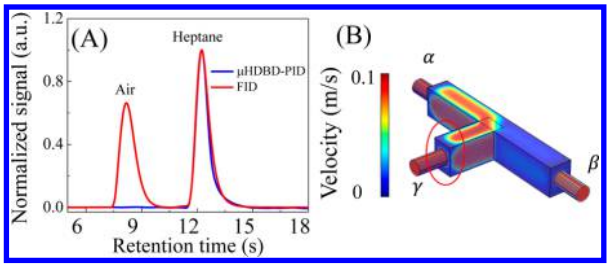

Figure 7. (A) Normalized signal obtained with μHDBD-PID and FID. Carrier gas flow rate was 1 mL/min. Auxiliary flow pressure was 1 psi. fwhm of 0.85 s and 0.72 s was obtained, respectively, for μHDBD-PID and FID. A 1 m Rtx-1 column was used for air and heptane separation. (B) COMSOL Multiphysics 3D simulation of helium flow with an auxiliary helium flow rate of 5.8 mL/min from inlet α and a carrier gas flow rate of 1 mL/min from inlet β. Outlet γ serves a common outlet with 101.35 kPa. The internal chamber volume is estimated to be 1.4 μL, and the dead volume, defined as the region having a helium flow velocity less than 0.1 m/s, is estimated to be 6 nL (see the circled part).

internal chamber volume was only 1.4 μL, corresponding to an ultimate peak width as sharp as 56 ms (calculated from the gas swept time with a 1.5 mL/min flow rate). The dead volume of the μHDBD-PID is estimated to be only 6 nL from the COMSOL simulation shown in Figure 7(B); thus, the tailing effect can be negligible. We further characterized the response time of the μHDBD-PID in Figure S5 using VOCs with lower volatilities (C_8–C_{12}, vapor pressure at 25 °C: ~1500 Pa to 18 Pa). In this case, the μHDBD-PID was placed outside the GC oven and at room temperature, and connected to a 7 m long separation column (Rtx-VMS) via a 1 m long guard column, whereas the commercial FID was directly connected to the above separation column (Rtx-VMS) and heated to 300 °C. The comparison results are given in Figure S5, showing no difference in the peak width for C_8–C_{12}. Therefore, our μHDBD-PID can be safely used at room temperature to analyze VOCs with volatility higher than C_{12} (vapor pressure = 18 Pa at 25 °C), which helps save the energy for detector heating. Later, we will show that our μHDBD-PID is able to detect VOCs with even lower vapor pressure without the condensation effect (see the section "Application to GC Separation").

Linearity. In order to perform an accurate quantitative analysis, linear response to analyte is highly desirable. Here, the peak height response curves of eight representative analytes with injection masses in a range from a few tens of picograms to a few tens of nanograms (limited by the sample capacity of the separation column, which is a couple of hundred nanograms) are shown in Figure 8, showing an excellent linearity (see Table S2 for the linear regression parameters). Considering the detection limit of only a few picograms for the above analytes (see next section), a linear dynamic range of >4 orders of magnitude can be obtained.

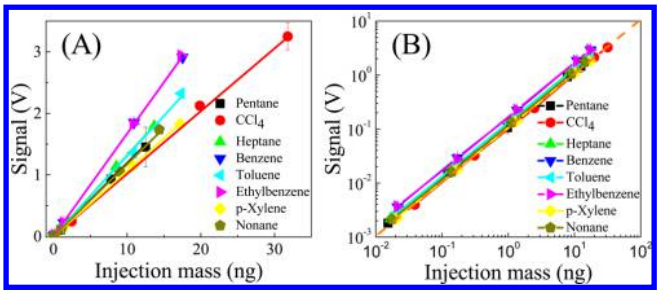

Figure 8. μHDBD-PID linearity test for eight VOCs. (A) Peak height as a function of injection mass in the linear–linear scale. Solid curves are linear fits with the related parameters given in Table S2. (B) The corresponding data and curves in (A) plotted on the log–log scale. The dashed line shows the curve with a unity slope to guide the eye. The slope of each curve is 0.9979, 1.0205, 1.00103, 0.99626, 0.99403, 0.99491, 0.99807, and 0.99845 from pentane to nonane, respectively. Error bars were obtained with four measurements. Auxiliary flow pressure was 1 psi.

Detection Limit. The detection limit was calculated at 3 standard deviations based on the result of minimum injection mass in the above linearity tests (see Figure S7). The detection limits and physical properties of the eight VOCs are shown in Table 1.

Table 1. Detection Limits Parameters and Physical Properties[40] of Eight VOCs

VOC	DL[a]	IP[b]	PH[c]	SD[d]
Pentane	4.6	10.35	1.81	0.3
CCl_4	5.3	11.47	3.95	0.25
Heptane	4.2	10.08	2.19	0.21
Benzene	3.2	9.25	3.64	0.04
Toluene	4.0	8.82	2.85	0.04
Ethylbenzene	3.1	8.76	3.71	0.03
p-Xylene	5.1	8.56	2.26	0.04
n-Nonane	4.5	9.72	2.13	0.04

[a]Detection limit at 3σ (pg), σ = 0.18 mV. [b]Ionization potential (eV). [c]Peak height (mV). [d]Standard deviation of peak height (mV) obtained with four measurements.

Here it is worth discussing the design in our μHDBD-PID that helps improve the detection limit. First, the analyte channel and helium discharge channel in the μHDBD-PID are fluidically separated (see Figure 7(B)), which prevents the analyte dilution caused by the incoming auxiliary flow. Second, the electrodes of the μHDBD-PID are composed of the entire sidewall of the p-type silicon wafers. Such a long electrode (6 mm) along the UV illumination pathway facilitates the low detection limit. Similarly, in recent studies,[10,26] multiple collection electrodes were used to improve the sensitivity.

DOI: 10.1021/acs.analchem.6b02180
Anal. Chem. 2016, 88, 8780–8786

Third, the small gap of only 380 μm between the two electrodes ensures efficient collection of ions and electrons generated by photoionization.

Application to GC Separation. In Figures 9 and 10, the overall performance of the μHDBD-PID was tested by

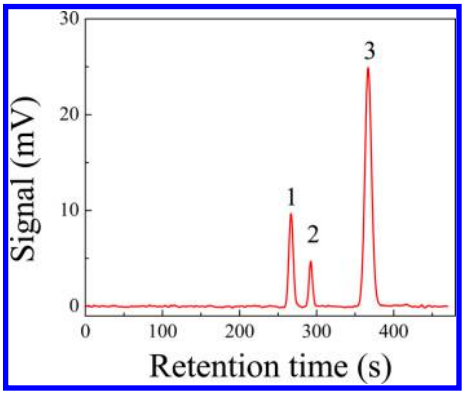

Figure 9. μHDBD-PID detection of permanent gases: (1) Hydrogen (30% V/V); (2) Oxygen (10% V/V); and (3) Nitrogen (60% V/V), with a total injection volume of 10 μL via gastight syringes with shut-off valves (50R-V-GT, SGE) and a spilt ratio of 100. Separation was achieved by using a 30 m Mol Sieve 5A PLOT column (320 μm ID and average coating thickness of 15 μm) at a helium flow rate of 1 mL/min and isothermal condition (35 °C).

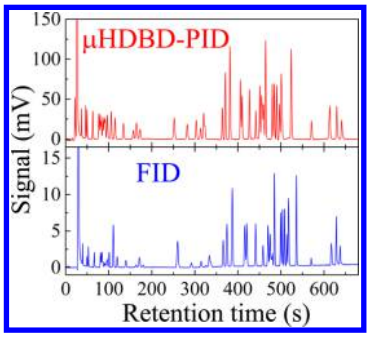

Figure 10. 0.1 μL (with a 100 split ratio) EPA 8260 VOC mixture (purchased from Sigma-Aldrich P/N 500607, containing 51 analytes) with 47 VOC peaks detected by both μHDBD-PID and FID. The four remaining VOCs were coeluted. Separation was achieved by using a using a 7-m long Rtx-VMS column at a carrier flow rate of 1 mL/min. Temperature ramping: T = 35 °C for 4 min and then to 160 °C at a rate of 18 °C/min. The names of the 51 VOCs can be found in Table S3.

detecting permanent gases and EPA 8260 standard reagent, respectively. The mixture of the permanent gases (hydrogen, nitrogen, and oxygen) was prepared in a Tedlar bag and separated with a PLOT column. Even though the ionization potential of nitrogen is as high as 15.58 eV, it can still be ionized and detected by the μHDBD-PID, which substantiates the universal applicability of our detector. There are 51 VOCs in a sublist of the EPA 8260 standard reagents. Figure 10 shows the comparison between FID (heated to 300 °C) and μHDBD-PID (operated at room temperature), with 47 peaks being fully separated and detected by both detectors (see also Figures S8 and S9 for some of the exemplary peaks and Table S3 for the names of the 51 VOCs). Except for the four coeluents, all the separated eluents exhibit the symmetric peak shape and comparable peak width for both detectors. Particularly, Figure S9 shows the last two analytes (naphthalene and 1,2,3-trichlorobenzene) in the chromatogram, which are actually #96 and #97 analyte in the EPA 8260 list and have a vapor pressure of 11.3 and 28 Pa, respectively, at 25 °C. Comparison between the two detectors shows no difference in their respective peak widths, suggesting that the μHDBD-PID is able to handle the VOCs with the vapor pressure as low as 10 Pa and up to naphthalene and 1,2,3-trichlorobenzene in the EPA 8260 list without the condensation issue.

Nondestructive Evaluation and Long-Term Operation Evaluation. We tested the nondestructive nature of the μHDBD-PID in Figure S10, in which the FID was connected to the μHDBD-PID via a 40 cm guard column. The peak height of the FID was compared by turning the μHDBD-PID plasma "ON" and "OFF", and it was found to be same with a t test. Finally, the μHDBD-PID exhibited excellent robustness. No single failure was observed during 3-week long operation.

CONCLUSION

We have developed a novel μHDBD-PID that exhibits superior characteristics and performance in size, weight, ease of fabrication, cost, power consumption, detection limit, dynamic range, response time, and detector lifetime. It can be broadly used in portable and micro-GC systems for *in situ*, real time, and sensitive gas analysis.

ASSOCIATED CONTENT

Supporting Information

The Supporting Information is available free of charge on the ACS Publications website at DOI: 10.1021/acs.analchem.6b02180.

Detailed comparison of our μHDBD-PID with other HD-PIDs, 3-view diagram of the μHDBD-PID, circuitry for helium discharge plasma excitation, picture of the power supply, circuitry for signal read-out, signal–retention time–flow rate curve, signal–retention time curves, peak height/injection mass–log(injection mass) plot, linear regression parameters of 8 VOCs, μHDBD-PID detection of VOCs, and names of the 51 VOCs used in Figure 10 (PDF)

AUTHOR INFORMATION

Corresponding Author

*Email address: xsfan@umich.edu.

Notes

The authors declare no competing financial interest.

ACKNOWLEDGMENTS

We would like to thank Environmental Protection Agency (83564401), the Michigan Center for Wireless Integrated MicroSensing & Systems for financial support, and Lurie Nanofabrication Facility for fabrication assistance.

REFERENCES

(1) Driscoll, J. N. *J. Chromatogr. A* **1977**, *134*, 49–55.
(2) Zhu, H.; Nidetz, R.; Zhou, M.; Lee, J.; Buggaveeti, S.; Kurabayashi, K.; Fan, X. *Lab Chip* **2015**, *15*, 3021–3029.
(3) Zhou, M.; Lee, J.; Zhu, H.; Nidetz, R.; Kurabayashi, K.; Fan, X. *RSC Adv.* **2016**, *6*, 49416–49424.
(4) Lee, J.; Zhou, M.; Zhu, H.; Nidetz, R.; Kurabayashi, K.; Fan, X. *Analyst* **2016**, *141*, 4100.
(5) Forsyth, D. S. *J. Chromatogr. A* **2004**, *1050*, 63–68.

DOI: 10.1021/acs.analchem.6b02180
Anal. Chem. 2016, 88, 8780–8786

(6) Jin, Q.; Yang, W.; Yu, A.; Tian, X.; Wang, F. *J. Chromatogr. A* **1997**, *761*, 169−179.
(7) Narayanan, S.; Rice, G.; Agah, M. *Sens. Actuators, B* **2015**, *206*, 190−197.
(8) Akbar, M.; Shakeel, H.; Agah, M. *Lab Chip* **2015**, *15*, 1748−1758.
(9) Lasa, J.; Mochalski, P.; Pusz, J. *J. Chromatogr. A* **2004**, *1035*, 261−264.
(10) Cai, H.; Stearns, S. D. *J. Chromatogr. A* **2013**, *1284*, 163−173.
(11) Cai, H.; Wentworth, W. E.; Stearns, S. D. *Anal. Chem.* **1996**, *68*, 1233−1244.
(12) Gremaud, G.; Wentworth, W.; Zlatkis, A.; Swatloski, R.; Chen, E.; Stearns, S. D. *J. Chromatogr. A* **1996**, *724*, 235−250.
(13) Mowry, C. D.; Pimentel, A. S.; Sparks, E. S.; Moorman, M. W.; Achyuthan, K. E.; Manginell, R. P. *Anal. Sci.* **2016**, *32*, 177−182.
(14) Sun, K.; Wentworth, W. E.; Stearns, S. D. *J. Chromatogr. A* **2000**, *872*, 141−165.
(15) Wentworth, W.; Sun, K.; Zhang, D.; Madabushi, J.; Stearns, S. D. *J. Chromatogr. A* **2000**, *872*, 119−140.
(16) Winniford, B. L.; Sun, K.; Griffith, J. F.; Luong, J. C. *J. Sep. Sci.* **2006**, *29*, 2664−2670.
(17) Wentworth, W. E.; Huang, J.; Sun, K.; Zhang, Y.; Rao, L.; Cai, H.; Stearns, S. D. *J. Chromatogr. A* **1999**, *842*, 229−266.
(18) Wentworth, W. E.; Cai, H.; Stearns, S. *J. Chromatogr. A* **1994**, *688*, 135−152.
(19) Wentworth, W. E.; D'Sa, E. D.; Cai, H.; Stearns, S. *J. Chromatogr. Sci.* **1992**, *30*, 478−485.
(20) Han, B.; Jiang, X.; Hou, X.; Zheng, C. *Anal. Chem.* **2014**, *86*, 936−942.
(21) Li, C.; Jiang, X.; Hou, X. *Microchem. J.* **2015**, *119*, 108−113.
(22) Li, W.; Zheng, C.; Fan, G.; Tang, L.; Xu, K.; Lv, Y.; Hou, X. *Anal. Chem.* **2011**, *83*, 5050−5055.
(23) Meyer, C.; Müller, S.; Gurevich, E.; Franzke, J. *Analyst* **2011**, *136*, 2427−2440.
(24) Bogaerts, A.; Neyts, E.; Gijbels, R.; van der Mullen, J. *Spectrochim. Acta, Part B* **2002**, *57*, 609−658.
(25) Narayanan, S.; Rice, G.; Agah, M. *Microchim. Acta* **2014**, *181*, 493−499.
(26) Manginell, R. P.; Mowry, C. D.; Pimentel, A. S.; Mangan, M. A.; Moorman, M. W.; Sparks, E. S.; Allen, A.; Achyuthan, K. E. *Anal. Sci.* **2015**, *31*, 1183−1188.
(27) Golubovskii, Y. B.; Maiorov, V. A.; Behnke, J.; Behnke, J. F. *J. Phys. D: Appl. Phys.* **2003**, *36*, 39.
(28) Na, N.; Zhang, C.; Zhao, M.; Zhang, S.; Yang, C.; Fang, X.; Zhang, X. *J. Mass Spectrom.* **2007**, *42*, 1079−1085.
(29) Gras, R.; Luong, J.; Monagle, M.; Winniford, B. *J. Chromatogr. Sci.* **2006**, *44*, 101−107.
(30) Na, N.; Zhao, M.; Zhang, S.; Yang, C.; Zhang, X. *J. Am. Soc. Mass Spectrom.* **2007**, *18*, 1859−1862.
(31) Kuklya, A.; Engelhard, C.; Uteschil, F.; Kerpen, K.; Marks, R.; Telgheder, U. *Anal. Chem.* **2015**, *87*, 8932−8940.
(32) Jafari, M. T. *Anal. Chem.* **2011**, *83*, 797−803.
(33) Andrade, F. J.; Shelley, J. T.; Wetzel, W. C.; Webb, M. R.; Gamez, G.; Ray, S. J.; Hieftje, G. M. *Anal. Chem.* **2008**, *80*, 2646−2653.
(34) Shinada, K.; Horiike, S.; Uchiyama, S.; Takechi, R.; Nishimoto, T. *Shimadzu Hyoron* **2012**, *69*, 255−263.
(35) Sun, G.; Liu, W.; Li, C.; Zhang, R. *JPCS* **2013**, *441*, 012023.
(36) Johnson, G. L. *Inductors and Transformers*; Kansas State University: 2001.
(37) Corke, T. C.; Enloe, C. L.; Wilkinson, S. P. *Annu. Rev. Fluid Mech.* **2010**, *42*, 505−529.
(38) Cheng, X.; Sherman, J.; Murphy, W.; Ratovitski, E.; Canady, J.; Keidar, M. *PLoS One* **2014**, *9*, e98652.
(39) Ravi, V.; Mok, Y. S.; Rajanikanth, B. S.; Kang, H.-C. *Fuel Process. Technol.* **2003**, *81*, 187−199.
(40) Haynes, W. M. *CRC Handbook of Chemistry and Physics*; CRC Press: 2014.

DOI: 10.1021/acs.analchem.6b02180
Anal. Chem. 2016, 88, 8780−8786